INTERNATIONAL JOURNAL OF MARITIME TECHNOLOGY
IJMT Vol.18/Spring & Summer 2023 (1-14)
Available online at: www. ijmt.ir

Numerical and experimental investigation of the hydrodynamic Lift and Drag coefficients of a solar-powered AUV in near-surface mode

Asadi Asrami. Ehsan[1*], Moonesun Mohammad[2]

[1]*Azad University of Takestan, Department of Energy Conversion, easadiasrami@gmail.com*
[2] *Assistant Professor, Shahrood University of Technology, Faculty of Civil Engineering, m.moonesun@gmail.com*

ARTICLE INFO

Article History:
Received : 15 Feb 2023
Accepted : 17 Apr 2023

Keywords:
Times New Roman 9
Times New Roman 9
Up to 5 Phrases

ABSTRACT

To obtain the hydrodynamic forces acting on a solar-powered AUV, and to investigate the effects of the free surface, a model of this type of vessel was simulated in ANSYS FLUENT 18 commercial software. To validate the data, a vessel with a scale of 1: 1 compatible with the installation of photovoltaic panels was built and tested in the towing tank of the National Iranian Marine Laboratory (NIMALA). The standard k-ε model and multi-block mesh were used to simulate the three-dimensional unsteady viscous flow around these cases: individual struts, the body without struts, and the body with struts. Three depth-to-diameter ratios ($\frac{h}{d} = 3.6\,.\,4.5\,.\,5.2$) and six Froude numbers in the range of $0.06 \sim 0.35$, equivalent to the Reynolds range 2.4×10^{05} to 1.4×10^{06}, were used to obtain lift and drag coefficients. The findings of this study were used to create a solar AUV. The maximum percentage of struts contribution in the total resistance force is 62 percent. The generated resistance effect, caused by struts and their attachment to the body, also plays a significant role. According to the current study data for the analyzed model, its maximum value is around 41 percent.

1. Introduction

Autonomous underwater vehicles (AUVs), are self-propelled vehicles that can inspect ship bottoms and seabed pipes, map sea-beds, oceans, and lakes, and undertake climate research, among other tasks. They act in places or situations where human presence is risky, expensive, or impossible to finance [1]. The development, production, and use of these AUVs face a number of challenges, including routing, navigation, programming, and so on. The stability of the energy source employed, which allows the vessel to execute long-term missions, is one of the primary issues of this type of vehicle. Today's AUVs are powered by a variety of lithium-polymer or lithium-ion batteries that are charged from the starter's energy source. As a result, the endurance of these vessels is determined by the battery charge. For such vessels, using a reliable and accessible energy source can be advantageous. The most common, clean, efficient, and accessible energy source for AUVs is solar energy.

To introduction the solar AUVs, there are some papers and texts, such as: a solar system for long-term use in AUVs [2], [3]. The evaluation and testing results of a solar AUV and its subsystems were provided in [4]. Long-term ocean sampling with a solar-powered AUV was examined by [5]. They looked into the factors that go into designing an energy management system and how they affect the performance of an AUV. The findings of a long-term test of solar-powered AUVs were examined by [6]. Devised and manufactured a solar-powered AUV that is light and portable [7].

Due to the energy constraints on such vessels, precise energy estimation is required. Calculating the forces operating on the vessel is vital to determine the required energy for moving and maneuvering the vessel in various missions and conditions in surface and subsurface modes. In the last two decades, researchers have concentrated on CFD-based approaches and comparing results to laboratory data when researching the hydrodynamic behavior of surface and subsurface vessels. There are few published scientific articles about the hydrodynamic effects on a submerged body near the free surface, such as characterization of near surface effects acting on an underwater vehicle by [8], experimental investigation into the hydrodynamic characteristics of a submarine operating near the free surface by [9]. Numerical hydrodynamics of flow on an AUV moving near the surface concerning the laminar-turbulent flow transition investigated in [10]. They investigated hydrodynamic coefficients in non-dimensional depths of 0.75 to 4D, for near surface

movement. They solved RANS equations by finite volume method and VOF method used to model the free surface effects. To simulate turbulence flow, two models were applied, $k-\varepsilon$, $k-\omega\,SST$. Obtained results indicate, $k-\omega\,SST$ model, show better consistency with experimental results. CFD and laboratory findings to investigate the lift and drag coefficients of an AUV used in [11]. The paper investigates hydrodynamic coefficients at various relative submergence depths at AUV speeds of 1.5 and 2.5 $\frac{m}{s}$. They studied the effect of free surface with and without presence of struts. Drag coefficients obtained from two phase flows simulations are compared with those obtained from single phase flows at corresponding values. The hydrodynamic parameters of a solar-powered AUV in surface-motion mode were studied by [12]. They ran a CFD simulation and compared the findings with experimental data. The following studies can be mentioned about using numerical simulation to analyze the underwater vessel motion: hydrodynamic analysis of a solar AUV body by [13]. Investigating the near-surface motion behavior of a submarine, simulating the hydrodynamic characteristics using CFD and comparing it with laboratory data [14]. They studied the effect of free surface on the hydrodynamic forces of the hull at a submerged depth equal to the diameter of the submarine model. The main point in their work is to investigate the effect of struts on the total resistance of the vessel and estimate the induced resistance caused by struts. This type of resistance is due to the connection of the struts to the body. They found that: this resistance can be up to 70% of total resistance.

Some researches were done about the NACA 0012 and 0015 sections near the free surfaces. Using asymmetric submerged hydrofoils in surface mode to simulate water waves investigated in [15]. The NACA4412 hydrofoil and the FLUENT commercial code were utilized in this simulation. Using the volume of fluid (VOF) method to numerical simulate of the free surface of a water wave flow around a NACA0015 hydrofoil was carried out in [16]. For validation, they initially ran a two-dimensional simulation of NACA0012 and compared the results of drag and lift forces, as well as wave height, to the available data, before running the same simulation on the NACA0015 hydrofoil. The FLUENT commercial code was used in this study. Using the OpenFOAM algorithm, by [17] they simulated the free surface flow around the NACA0012, a 2D hydrofoil.

The results of the DARPA SUBOFF submarine test have been reported in many studies, including [18] and [19].

A solar AUV, firstly in surface mode, absorbs solar radiation through its photovoltaic panels; when its batteries are charged, it sinks in the water for various missions. To estimate AUV required energy, we have to evaluate hydrodynamic forces acting on the AUV's body for a test model. The flow around an AUV that uses a solar energy source is explored in this study. A 1: 1 scale model of this form of vehicle was created and built out of Abies (fir) wood, and after final surface polishing and painting, it was tested at the National Iranian Marine Laboratory (NIMALA). The two wings were each based on the NACA0015 cross-sectional profile to create a proper lift and place the panels. The four astern hydroplanes at a 90-degree angle to each other were likewise built from the same section. The center body was a SUBOFF model as well. The simulation results for three depth-to-diameter ratios with varying diameters ($\frac{h}{d}=3.6\,.4.5\,.5.2$), and in the Reynolds number range (calculated in terms of body length) $Re=2.4\times10^{5}\sim1.4\times10^{6}$, and the results were compared using the FLUENT 18 commercial code. The forces acting on the two struts, as well as the forces acting on the body without the struts, were calculated individually and independently by numerical simulation to get the net forces operating on the model body. The resistance force was lower in both the body without struts and the individual struts cases than in the body with struts. This difference is due to the induced resistance force. The lift forces caused by the presence of extended wings (which are where photovoltaic panels are installed) and astern hydroplanes were also examined using the CFD method, and the shapes of the wave profiles derived from the CFD method and test at any speed and depth were also compared. In figure (1-a), the test model is shown, without struts (right side), and attached to struts (left side), and in figure (1-b), the prototype which made by Falmouth company is shown when it's prepared to launch.

(a)

(b)

Figure (1): (a): Solar AUV to test in NIMALA towing tank and (b) a real type of solar powered AUV, is prepared to launch

2. Governing equations:

The flow around the solar AUV was solved using the Navier-Stokes equations of unsteady flow (URANS) to obtain drag and lift coefficients. The first equation is the continuity or mass conservation equation. The following is an equation for mass conservation. Following equations are written in tensor form:

$$\frac{\partial \rho}{\partial t} + \frac{\partial}{\partial x_i}(\rho u_i) = 0 \quad (1)$$

The following is the momentum conservation equation, which is written as follows:

$$\frac{\partial(\rho u_i)}{\partial t} + \frac{\partial(\rho u_i u_j)}{\partial x_i} = \frac{\partial \tau_{ij}}{\partial x_j} - \frac{\partial p}{\partial x_i} + \frac{\partial}{\partial x_j}\left(-\rho\overline{u_i' u_j'}\right) \quad (2)$$

$$\tau_{ij} = \mu\left[\left(\frac{\partial u_i}{\partial x_j} + \frac{\partial u_i}{\partial x_i}\right) - \frac{2}{3}\delta_{ij}\frac{\partial u_l}{\partial x_l}\right] \quad (3)$$

$$-\rho\overline{u_i' u_j'} = \mu_t\left(\mu\frac{\partial u_i}{\partial x_j} + \frac{\partial u_j}{\partial x_i}\right) - \frac{2}{3}\left(\rho k + \mu_t\frac{\partial u_k}{\partial x_k}\right) \quad (4)$$

The volume of fluid (VOF) method is used to simulate the free surface's shape due to the vessel's movement beneath the water surface. First utilized this method to calculate the surface wave created by a submerged hydrofoil moving toward a free surface [20]. The volume fraction of each fluid in each computational cell is traced along the domain using an equation concerning the solution of the flow field. This method's governing equation is as follows:

$$\frac{D\vec{F}}{Dt} = \frac{\partial F}{\partial t}(\vec{x}.t) + \left(\vec{V}.\nabla\right)F(\vec{x}.t) = 0 \quad (5)$$

Where *F* is equal to one, it is occupied completely by the fluid and zero indicates other locations, it equals the volume fraction of the fluid-occupied cell when averaged throughout a computational cell. A value of 1 for *F* implies that the cell is filled with fluid, whereas a value of zero indicates that the cell is empty. Inside the cell, values between *0* and *1* represent a free surface. Two-fluid and two-phase approaches are utilized in this study; therefore, a value of *1* for *F* indicates that the computational cell is filled with water, and a value of zero indicates that the computational cell is filled with air. Values between *0* and *1* represent the free level. The standard k - ε turbulence model is used to simulate the turbulence. This method is based on semi-empirical modeling for the kinetic energy transfer equations k and its dissipation rate, ε. The values of k and ε are obtained as follows:

$$\frac{\partial(\rho k)}{\partial t} + \frac{\partial(\rho k u_i)}{\partial x_i} = \frac{\partial}{\partial x_j}\left[\left(\mu + \frac{\mu_t}{\sigma_k}\right)\frac{\partial k}{\partial x_j}\right] + G_k + G_b - \rho\epsilon - Y_m + S_k \quad (6)$$

And

$$\frac{\partial(\rho\epsilon)}{\partial t} + \frac{\partial(\rho\epsilon u_i)}{\partial x_i} = \frac{\partial}{\partial x_j}\left[\left(\mu + \frac{\mu_t}{\sigma_\epsilon}\right)\frac{\partial \varepsilon}{\partial x_j}\right] + C_{1\varepsilon}\frac{\varepsilon}{k}(G_k + C_{3\varepsilon}G_b) - C_{2\varepsilon}\rho\frac{\varepsilon^2}{k} + S_\epsilon \quad (7)$$

Where G_k is the kinetic energy produced by the mean velocity gradient, G_b is the kinetic energy produced by buoyancy, and Y_m is the contribution of expansion oscillation to compressible turbulence at the rate of total dissipation. $C_{1\varepsilon}$,$C_{2\varepsilon}$, $C_{3\varepsilon}$ are the constants. The turbulence Prandtl numbers σ_k and σ_ϵ a correspond to k and ε, respectively. S_k and S_ϵ are source terms that have been defined by the user. The combination of k and ε defines turbulent viscosity μ_t, as follows:

$$\mu_t = C_\mu\frac{k^2}{\epsilon} \quad (8)$$

Where C_μ is constant. Also we define two non-dimensional parameters that are characteristics of the flow regime. Reynolds number that helps predict fluid flow patterns in different situations by measuring the ratio between inertial and viscous forces. At low Reynolds numbers, flows tend to be dominated by laminar (sheet-like) flow, while at high Reynolds numbers, flows tend to be turbulent.

$$Re = \frac{vl}{\vartheta} \quad (9)$$

Where v is the flow velocity and l is the characteristic length and ϑ is the kinematic viscosity. And Froude number is a ratio of inertial and gravitational forces. Inertia (denominator) - reflects its willingness to do so. The Froude number is a measurement of bulk flow characteristics such as waves, sand bed-forms, flow/depth interactions at a cross section or between boulders.

$$Fn = \frac{v}{\sqrt{gl}} \quad (10)$$

Where v is the flow velocity and l is the characteristic length and g is the gravitational acceleration. In this work, we consider l as the length of vehicle to determine the Reynolds number, and for Froude number in simulations of individual SUBOFF body and body attached to the struts and the strut diameter for simulation of individual strut mode. We define the coefficient that is defined similarly either for pressure and drag and lift coefficients.

$$C = \frac{F}{0.5\rho v^2 A} \qquad (11)$$

Where C is the coefficient, F is the force (drag and lift), for defining the C_p it changes to p, the flow pressure, ρ is the fluid density, v is the flow velocity and A is the wetted area.

3. Experimental procedure of model resistance assessment

To achieve the characteristics of the resistance and the waveform formed during the test of the studied model, a model made of Abies was constructed by CNC lathes with a 1:1 scale vessel, following the ITTC 7.5-02-03-01.4 (revision 04-2017) recommendations, and then the surface was polished and painted. For higher accuracy, the model's four astern hydroplanes were made utilizing the RP (rapid prototype) technique. The astern hydroplanes and the large wings, which act as mounting components for the photovoltaic panels, were built separately and then assembled into the body. The body linked to the struts can be seen in Figure (2). Because the body is made of wood, lead is used to fully immerse it. This lead addition is necessary to maintain balanced weight distribution in the vessel geometry. Struts are regulated in height to provide the possibility of their wetted height measurement.
measurement.

(a)

(b)

(c)

Figure (2): The manufacturing procedure of the model made of Abies : (a): machining the mid-body, (b): mid-body attached to the wings and polished, (c): completed, painted model

The model's movement within the towing tank is restricted to a single degree of freedom and a straight line. Struts connect the model to two two-component dynamometers (Figure 3). This laboratory's towing tank is 402 meters long, 6 meters wide, and 4.5 meters deep. Its trolley speed ranges from 0.1 to 19 m/s in two modes of motion: slow motion (0.5 to 5 m/s) and fast motion (4.5 to 19 m/s). The passenger trolley has a capacity of 5 people and dimensions of 7.6 7.6 meters. The model is towed at a constant pace at all six speeds and three depths during the test. The forces acting on the body and struts at each speed are measured with a force transducer and recorded on a computer.

Figure (3): A view of the NIMALA towing tank and model test attachment to the struts and 2-component force transducer

4. Model Description:

A solar AUV model is created using the dimensions indicated in the Figure (4) and table (1).

Table 1. Main dimensions of solar AUV and struts

AUV components	Dimensions (mm)
Overall length	1200
Width	860
Body middle section maximum diameter	140
Wing root chord length	614
Wingtip chord length	487
Wing camber thickness	52.66
Rudder root chord length	55.32
Rudder tip chord length	42
Rudder camber thickness	6.3
Maximum Strut Diameter	65
Minimum Strut Diameter	20
Strut Overall Height	1000

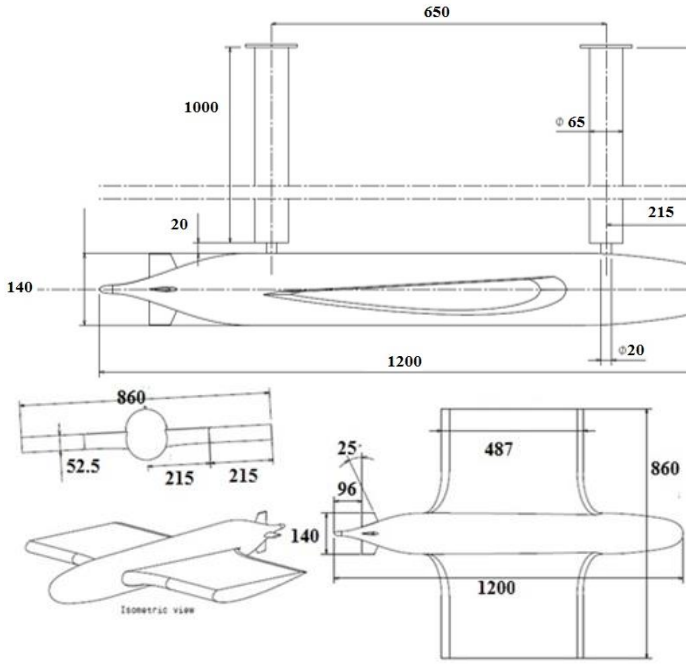

(a)

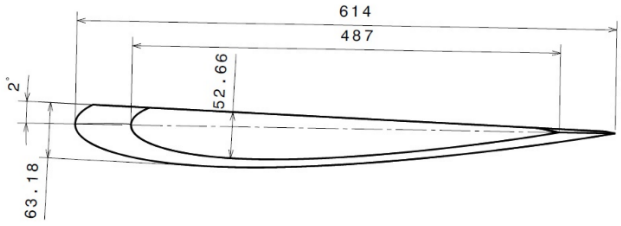

(b)

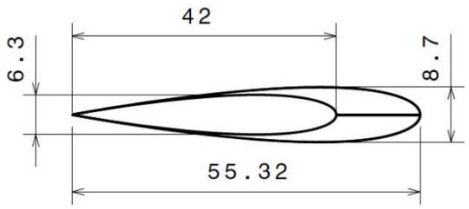

(c)

Figure (4): The model and attached struts (a), wing (b), and rudder (c) dimensions in mm.

5. CFD simulation

One of the most significant aspects of vessel modeling and analysis is choosing a computational domain that is appropriate for the type of problem. If the domain dimensions are incorrect, the results will be erroneous, and the solution time and computing costs will be increased. Figure (5) shows the solution domain for the body of the model as mentioned earlier attached to the struts. It has a length of *5 L*, a height of *1.6 L*, and a width of *2.8 L*. The model's body is placed at a distance of L from the inlet boundary, *3 L* from the outlet boundary, and as much as L in the direction of height from the surface of the cylindrical body of the SUB OFF model from the upper boundary and 0.2 L from the lower boundary, as recommended by the ITTC (7.5-03-02-03). Half of the body and the domain is modeled in the width direction, and the body is 1.4 L distant from the lateral boundary. Although the entire domain is shown in Figure (6), only half is solved. The SUB OFF model's dimensionless height of the free surface from the upper surface of the cylindrical body is$\frac{h}{d} = 3.6 . 4.5 . 5.2$, (the height to diameter ratio). Half of the domain and the model were evaluated to lower the computing cost due to the symmetry of the model geometry along the longitudinal line of the body and the domain. To solve the struts individually and the body independently, the same pattern is used in the domain dimensions. The pressure inlet and the pressure outlet boundary condition are considered in all three cases. The remaining boundaries are referred to as symmetry conditions. A wall boundary condition is also applied to the model's body. The upper boundary condition of the domain is treated as Pressure Outlet, air outlet, and atmospheric pressure conditions since the Open Channel Flow model was utilized in the selection of VOF model sub-models.

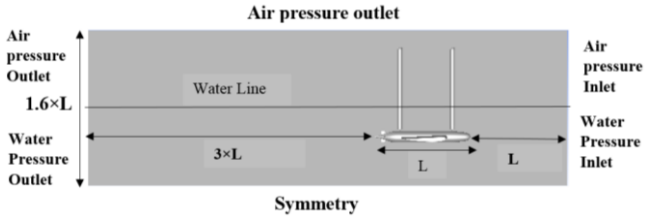

Figure (5): Domain dimensions and boundary conditions in the side view (X-Y plane)

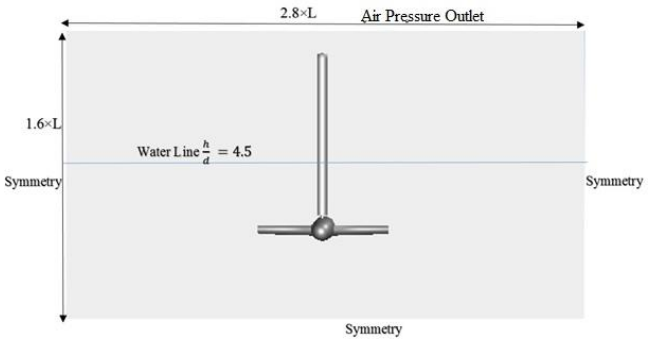

Figure (6): Full view of domain dimensions and boundary conditions in the front view (Y-Z plane) (solving is performed by half)

Table (2) specifies the step interval so that the Courant number is smaller than 1 in all cases. (The Courant number is a dimensionless value representing the time a particle stays in one cell of the mesh. It must be below 1 and should ideally be below 0.7. If the Courant number exceeds 1, the time step is too large to see the particle in one cell, it "skips" the cell.) Furthermore, coarser grids necessitate fewer time intervals. The time step begins with an estimate based on the ITTC 7.5-03-02-03 Recommendation based on body speed and keel wet length (L_k). The time step is calculated using the following:

$$\Delta t = 0.005 \sim 0.01 \times \frac{L_k}{V} \qquad (12)$$

During the simulation, the time step is adjusted as needed to meet the constraint that the Courant number is less than 1. The maximum number of iterations for each time step is 20. It's worth noting that the time step in the mode of solving the struts individually is equal to the distance between the beginning of the first strut and the end of the second strut, which is 0.715 m, but the same value of 1.2 m is used for single-body solutions and the body attached to the struts. The multi-block mesh method was utilized for meshing; an inter-domain block was formed around the body with a tetrahedral mesh, and a hex-wedge mesh was built around the struts. The planes composing the three-dimensional model are meshed independently and using the Tri-pave model to create improved density in the boundary layer. The other blocks are hexagonal grids constructed of hexahedral and hex-wedge hexagons that remove themselves from the body and struts and grow coarser in locations where the gradients are less or zero. To better simulate free surface changes, the grid density in the area that forms the free surface is raised as illustrated in Figure (7). When the model geometry is complex, using an unstructured mesh speeds up and simplifies the construction process, but also raises the computing cost and can impair the quality of the results. We increase the density of the unstructured mesh to improve the accuracy of the answer. However, by establishing a multi-block mesh and creating structured mesh in other sections of the domain, a balance between computing cost and accuracy in the answers can be achieved. Three cut views of the computational grid and an isometric view of the grid are shown in Figures (8) and (9).

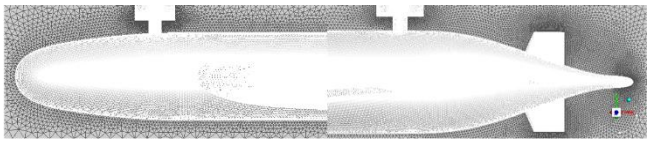

Figure (7): Mesh concentration of unstructured mesh at the bow and astern, and zones of attachment of struts to the body

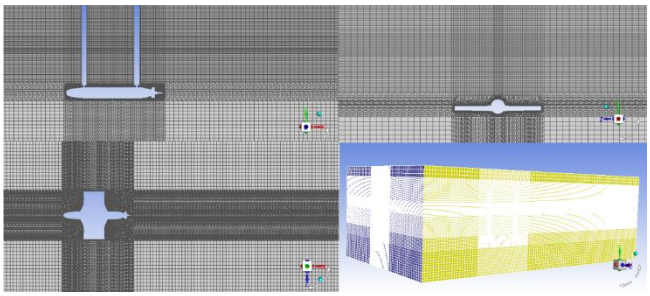

Figure (8): A multi-block grid generated around the attached model to the struts in the solution domain at three views and isometrics.

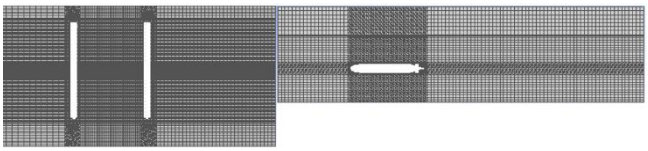

Figure (9): Cut view of the multi-block grid around the struts and the individual body model in the X-Y plane.

To achieve viscous flow effects in the boundary layer, tetrahedral mesh layers are created at the body surface to obtain high-quality mesh. The tetrahedral mesh parameters are also chosen so that the average wall y^+ on the body is around 50 (Azcueta [21]).Table (2) shows the values of changes in C_p, Cd, and y^+, as well as the time steps employed, for all three solution modes at Fn = 0.35 , $\frac{h}{d} = 3.6$, in six steps according to the getting finer mesh. We used different time steps in all three different modes of simulation to get better results according to the mesh independency. By the bigger time step values look like to coarse mesh, resulted Cd and C_p are more different to the final results that were obtained by finest mesh. The number

of computational cells for each step is $\sqrt{2}$ times that of the previous step (De Luca et al. [22]). The criterion values selected for solving are step 3 for table (2-a), step 4 for table (2-b), and step 5 for table (2-c). In table (a), for approximately 2.8 times the number of computational cells, from step three onwards, the C_p change is 1.2%, and it is 0.44% for C_d and 3.8% for y+. In table (b), the changes in C_p are 1.15 percent, 0.23 percent for C_d, and zero for y^+ for nearly doubling the number of computational cells from step four onwards. The value of the obtained C_d is compared to the value obtained from the experiment in the table (c). The difference between these two C_d values is 4.3 percent of the experimental value is used as the basis. It's also apparent that as the mesh gets finer, the time steps get more and more until they hit a fixed value. The graph of the Figure (10) depicts the trend of C_p changes. The y^+ values for the criterion states of the solution described in the tables are shown in Figure (11). The maximum value for C_p is found for the situation where the struts are analyzed individually. The lowest value is obtained for the case where the body is solved independently. The wave-making effect in the C_p values is the reason for this.

Table 2. Mesh independency in three forms of solutions (individual struts (a), individual body (b), struts attached to body (c))

(a) Struts mesh independency in Fn = 1.503 , $\frac{h}{d} = 7.7$

Step	1	2	3	4	5	6
Cell Numbers	159596	225705	318523	450459	637045	900919
C_p	0.072	0.069	0.066	0.065	0.065	0.065
C_d	0.076	0.071	0.068	0.068	0.068	0.068
Average y^+	87	66	52	51	51	50
Time Step (s)	0.0012	0.0021	0.0031	0.0031	0.0032	0.0032

(b) Body mesh independency Fn = 0.35 , $\frac{h}{d} = 3.6$

Step	1	2	3	4	5	6
Cell Numbers	215689	305031	431378	610062	862757	1220123
C_p	0.0091	0.0087	0.0081	0.0078	0.0077	0.0077
C_d	0.0152	0.0138	0.0134	0.0126	0.0126	0.0126
Average y^+	79	67	58	52	52	52
Time Step (s)	0.0035	0.0042	0.0048	0.005	0.0053	0.0053

(c) Body and struts mesh independency Fn = 0.35 , $\frac{h}{d} = 3.6$

Step	Experiment	1	2	3	4	5	6
Cell Numbers		283886	401476	567773	802952	1135546	1605904
C_p		0.037	0.034	0.031	0.029	0.025	0.026
C_d	0.038	0.045	0.043	0.042	0.041	0.036	0.036
Average y^+		75	71	63	55	50	49
Time Step (s)		0.0025	0.0033	0.004	0.0047	0.005	0.0051

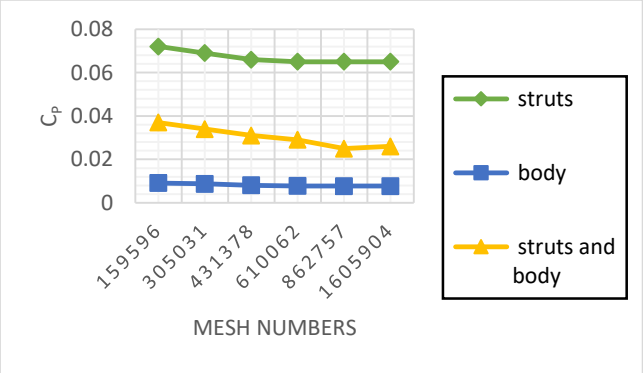

Figure 10. C_p variations versus mesh numbers

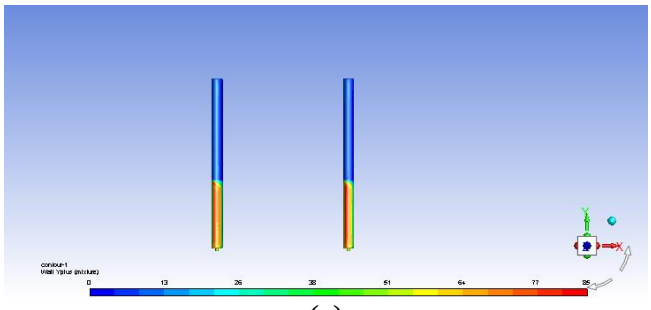

(a)

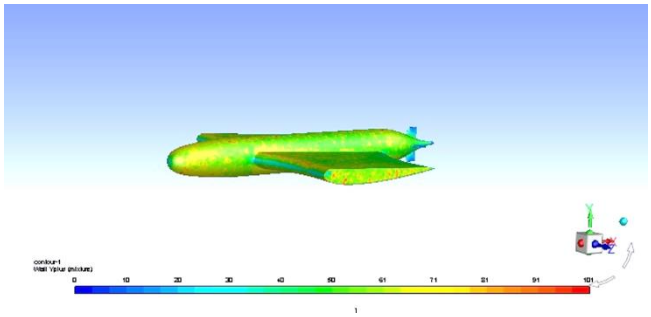

(b)

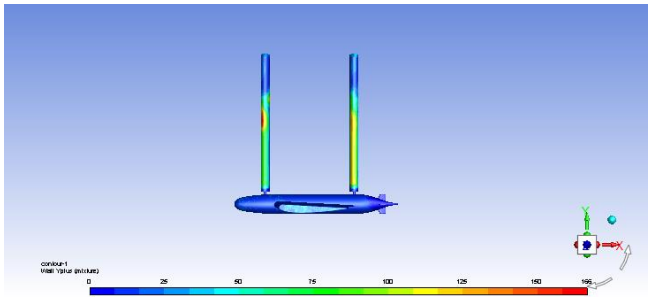

(c)

Figure 11. y^+ values for selected meshes at each solution form, struts (a) body (b) body and struts (c)

The simulation of this flow around the model is performed by the commercial code ANSYS FLUENT 18. In the inlet pressure boundary condition, the value of the fluid inlet velocity into the domain is equal to the value of the model velocity of the model as measured by the laboratory trolley. At the outlet pressure boundary, downstream of the flow, hydrostatic pressure is considered with respect to the calm water level. In both input and output boundary conditions, the height of the free surface from the base zero point and the lowest level of the domain from the same point is specified. In the input boundary condition for the water and air, turbulence characteristics for the input flow are given independently. The impact of water-air interface is considered using a constant surface tension value. The free surface of the flow surrounding the solar AUV was determined using computational fluid dynamics (CFD). The averaged Reynolds-Navier-Stokes unsteady equations (URANS) and the turbulence model standard k-ε are used, and near-wall behavior is the Standard Wall Function. This simulation employs the equation of the two-phase flow VOF model for two immiscible fluids, namely air and water. The dominant phase in this solution is air, whereas the secondary phase is water. Table (3) shows the parameters that were employed to solve this problem. It may be explained that in all three body solutions without struts, with the struts separated from the body, and with the body attached to the struts, all of the items mentioned in the numerical solution settings are the same.

Table 3. CFD settings

Parameter	Settings
Solver	3D, RANS, unsteady, implicit
Momentum discretization	Second order upwind
Pressure velocity coupling	SIMPLE
Multiphase flow model	Volume of fluid (VOF)
Phase Interaction	Surface tension force modeling, Wall adhesion
Turbulence Model	k-ε Standard
Wall treatment	Standard wall functions
Turbulent kinetic energy discretization	Second order upwind
Turbulence dissipation rate	Second order upwind
Models for body motions	Gravity, equations of motion
Degrees of freedom	Straight line motion
Time step criterion	Courant no. < 1.0
Number of inner iterations	20

6. Results and discussion

The results of the CFD solutions of the struts in the Froude range Fn = 0.25 ~ 1.5 in three depth to diameter ratios $\frac{h}{d} = 7.7\,.\,9.7.\,11.2$ are shown in Table (4). Where $\boldsymbol{h}$ is the immersion depth, water surface to the top surface of the vessel, and $\boldsymbol{d}$ is the maximum diameter of SUBBOF hull. It should be noted that the characteristic length is the diameter of a strut when computing the Froude number. The diameter value of the struts is considered when calculating the depth to diameter ratio $\frac{h}{d}$. The value of the total resistance coefficient for the strut remains relatively the same as the Froude number grows, as shown in the Table (4). Because from a certain velocity to the next (after the separation of the flow behind the struts), the pressure resistance coefficient and friction stay constant. However, when the depth-to-diameter ratio rises, so does the total resistance force coefficient. This is mostly due to an increase in the strut's wetted surface as a result of further immersion. The value of the total resistance coefficient does not change greatly with increasing Froude number at a constant ratio of depth to diameter, as can be seen in Figure (12). In contrast to the other two depth-to-diameter ratios, the value of the resistance coefficient increases at the depth-to-diameter ratio of 11.2, at Froude number 1.5. It diminishes at the same Froude number. This is due to the resistance coefficient's nonlinear behavior near the surface (for two lower depth to diameter ratios). The value of the resistance force coefficient can return to values corresponding lower speed values and be equal to them as the speed increases. The wave profile is shown in Figure (13) at a Froude number of 1.5 and a depth to diameter ratio of 7.7. The wave pattern created around the struts at Fn = 1.5, $\frac{h}{d} = 7.7$ is shown in this diagram. Maximum wave rising occurs in the forehead of each strut. It is higher by about 0.06 m in the front strut.

Table 4. Struts' resistance coefficients in three depth ratios versus Froude numbers

V (m/s)	Fn	C_d		
		$\frac{h}{d} = 7.7$	$\frac{h}{d} = 9.7$	$\frac{h}{d} = 11.2$
0.2	0.25	0.065	0.081	0.095
0.4	0.50	0.063	0.079	0.093
0.6	0.75	0.066	0.083	0.096
0.8	1	0.071	0.087	0.1
1	1.2	0.071	0.088	0.097
1.2	1.5	0.068	0.081	0.1

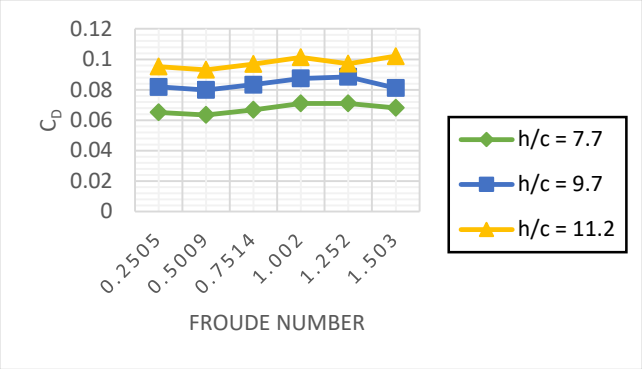

Figure 12. Struts' resistance coefficients variations in three depth ratios versus Froude numbers

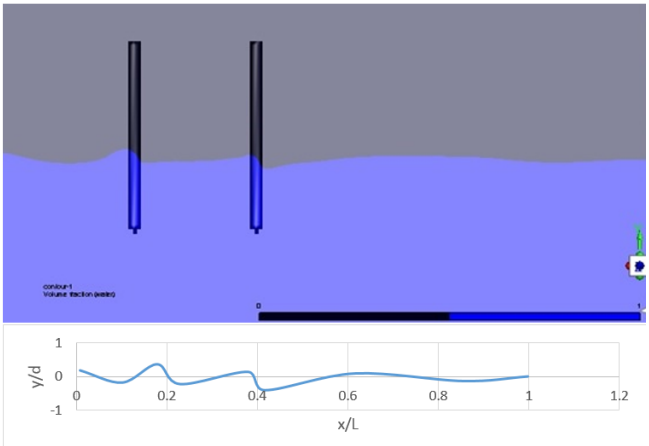

Figure 13. wave profile, water volume fraction and wave height in the domain, Fn = 1.5, $\frac{h}{d} = 7.7$ in Z = 0 plane

Table (4) shows the total resistance coefficients used by the CFD technique to calculate the flow around the solar AUV body without struts in the Froude number range Fn = 0.06~035, and three depth-to-diameter ratios of $\frac{h}{d} = 3.6, 4.5, 5.2$. The characteristic length is the length of the body when calculating the Froude number. Unlike the strut mode in Table (3) and the diagram in Figure (12), the vessel wetting area does not change with the ratio of depth to diameter in the flow solution mode around a single body. Figure (14) shows the decreasing trend of the total resistance coefficient as the Froude number increases for all three depth-to-diameter ratios and the proximity of the total resistance coefficient values to a fixed Froude number for three distinct depth-to-diameter ratios. The flow is laminar at lower velocities, and the viscous resistance force becomes the dominating resistance force, accounting for a more significant proportion of the total resistance force. The flow surrounding the body becomes more turbulent as the velocity increases. The proportion of pressure viscous resistance lowers as a result. The diagram also shows that the hydrodynamic forces obtained at this depth are independent of the free surface effect, even at the lowest depth-to-diameter ratio examined, $\frac{h}{d} = 3.6$ for the body independently from the struts (Jackson, H.A). As a result, the total resistance values stay mostly the same as the depth-to-diameter ratio increases. Because the resistance due to surface waves tends to zero for a depth-to-diameter ratio greater than 3, only frictional resistance and pressure viscosity remain.

Table 5. Body resistance coefficients in three depth ratios versus Froude numbers

V (m/s)	Fn	C_d		
		$\frac{h}{d} = 3.6$	$\frac{h}{d} = 4.5$	$\frac{h}{d} = 5.2$
0.2	0.06	0.021	0.021	0.021
0.4	0.11	0.015	0.015	0.016
0.6	0.17	0.014	0.014	0.013
0.8	0.23	0.013	0.014	0.012
1	0.29	0.012	0.012	0.012
1.2	0.35	0.012	0.013	0.01

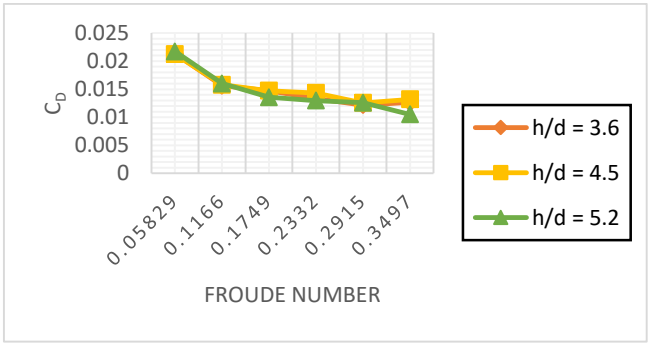

Figure 14. body resistance variations versus Froude numbers in three depth ratios

The lift coefficient decreases with increasing depth in the fixed Froude number, as seen in the table (5) and Figure (15). Due to the presence of a free surface, the pressure difference between the upper and bottom surfaces of the foil is reduced. The lift coefficient increases as the Froude number increases in the constant ratio of depth to diameter. The lift force increases as the Froude number grows because the foil has yet to attain the stall angle. The pattern and graph of free surface changes at $\frac{h}{d} = 3.6$ Fn = 0.35 are

shown in Figure (16). The highest point on the free surface is 0.097 m.

Table 6. Lift coefficients in three depth ratios versus Froude number

V (m/s)	Fn	C_l		
		$\frac{h}{d} = 3.6$	$\frac{h}{d} = 4.5$	$\frac{h}{d} = 5.2$
0.2	0.06	3	2.4	1.8
0.4	0.11	0.74	0.6	0.44
0.6	0.17	0.33	0.25	0.19
0.8	0.23	0.17	0.14	0.12
1	0.29	0.10	0.09	0.08
1.2	0.35	0.07	0.059	0.07

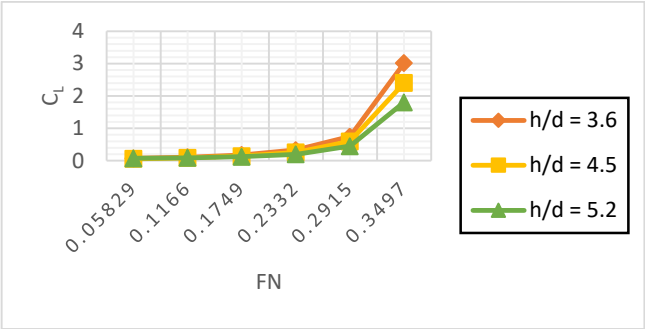

Figure 15. body lift variations versus Froude numbers in three depth ratios

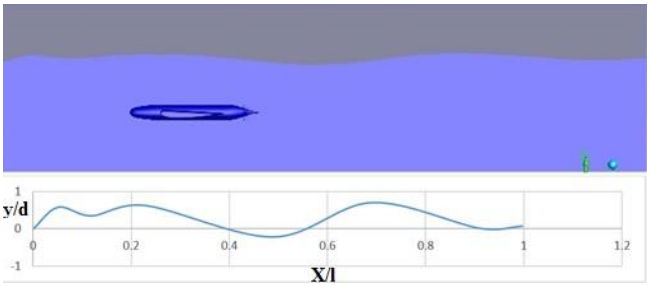

Figure 16. water volume fraction and wave height in the domain, Fn = 0.35, $\frac{h}{d} = 3.6$, Z = 0 plane

The results of the CFD flow solution for the motion state of the body attached to the struts are shown in table (7) and Figure (17). These results include lift and resistance coefficients. The Cd value decreases as the Froude number increases, but it is not tangible; it grows with an increasing depth-to-diameter ratio, primarily due to the increase in the wetted area of the struts. C_d values are also closer together when the Froude number grows for two depth-to-diameter ratios of 4.5 and 5.2 than for the ratio of depth-to-diameter of 3.6. It's also linked to a decrease in free surface and wave-making resistance influence when the depth-to-diameter ratio rises. This pattern differs from the resistance coefficient behavior observed earlier for a body without struts near the surface. The C_l coefficient increases with increasing Froude numbers, however for Froude numbers 0.29 and 0.35, this increase is accompanied by a sharp increase in slope, which is connected to Reynolds numbers and, accordingly, the flow's entry into a turbulent regime (Figure) (17)). At Fn = 0.35, $\frac{h}{d} = 3.6$, a wave pattern forms around the model, as shown in Figure (19). The free surface elevation is 0.07 m at its highest point. Figure (21) shows half of the model and domain to show the volume fracture of water at Fn = 0.35. Figure (23) compares free-surface wave elevations for CFD solution results and experimental testing.

Table (7) CFD hydrodynamic coefficients of body attached to struts

Fn	$\frac{h}{d} = 3.6$		$\frac{h}{d} = 4.5$		$\frac{h}{d} = 5.2$	
	C_d	C_l	C_d	C_l	C_d	C_l
0.06	0.043	0.063	0.052	0.055	0.063	0.043
0.11	0.039	0.098	0.051	0.085	0.057	0.073
0.17	0.037	0.16	0.05	0.14	0.05	0.12
0.23	0.037	0.30	0.044	0.26	0.049	0.22
0.29	0.037	0.70	0.044	0.61	0.052	0.53
0.35	0.036	2.85	0.042	2.5	0.048	2.2

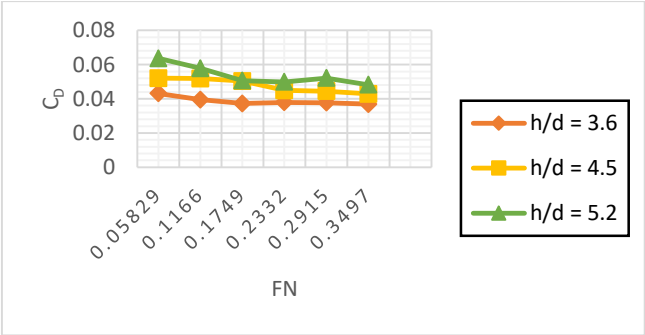

Figure 17. Body attached to struts resistance variations versus Froude numbers in three depth ratios

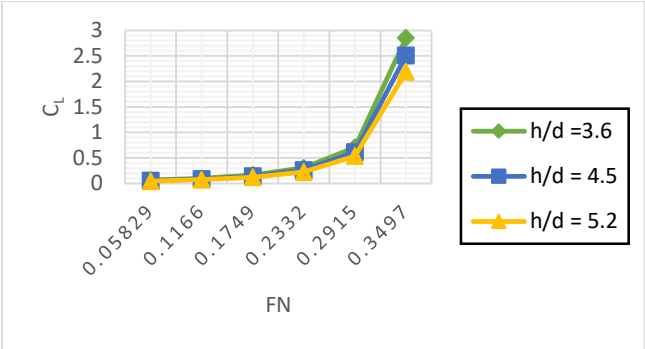

Figure 18. Body attached to struts, lift variations versus Froude numbers in three depth ratios

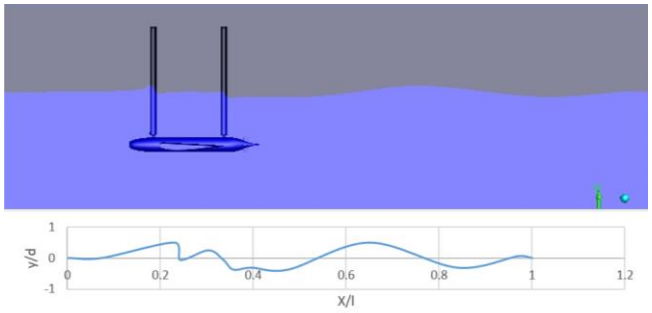

Figure 18. body attached to struts, lift variations versus Froude numbers in three depth ratios

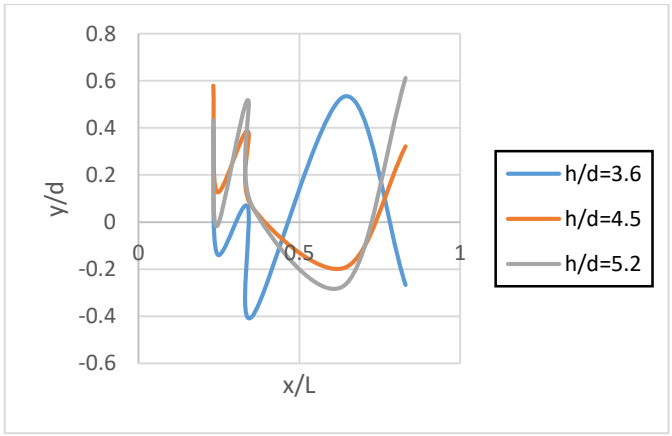

Figure 20. wave profile formed around the model and through the domain, Fn = 0.35

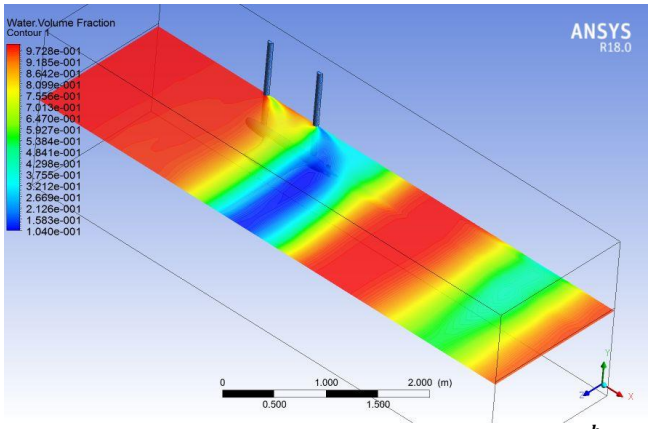

Figure 21. wave profile for body attached to the struts, $\frac{h}{d} = 3.6$, and Fn = 0.35, CFD results (half domain)

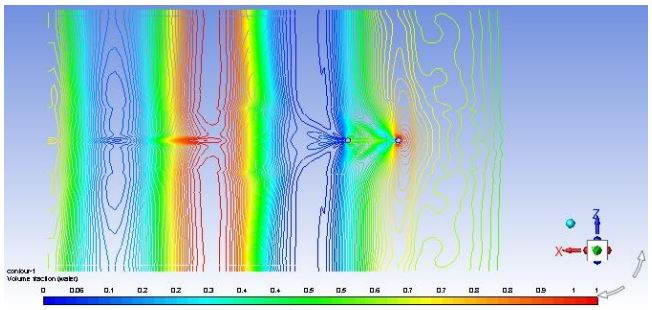

$\frac{h}{d} = 3.6$

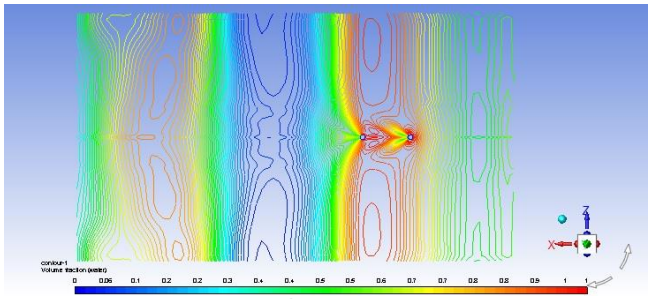

$\frac{h}{d} = 4.5$

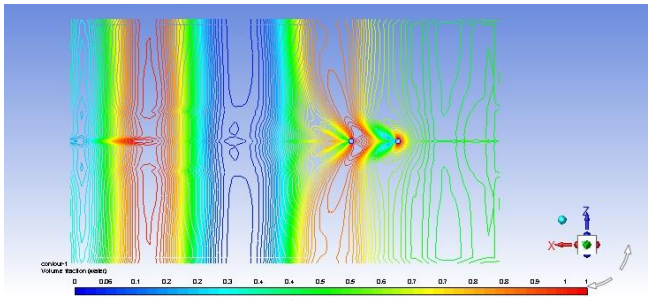

$\frac{h}{d} = 5.2$

Figure 22. wave pattern formed behind the struts attached to the body in Fn = 0.35

$\frac{h}{d} = 3.6$, and Fn = 0.35

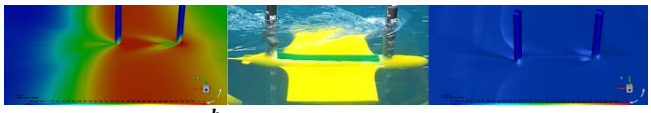

$\frac{h}{d} = 4.5$, and Fn = 0.35

$\frac{h}{d} = 5.2$, and Fn = 0.35

Figure 23. comparing the CFD and experimental wave patterns formed on the free surface in a magnified zone.

The pattern of static pressure distribution throughout the domain and surrounding the model is depicted in Figure (24). It has been observed that the same wave pattern forms at the free surface in low-pressure and high-pressure areas. The high-pressure region is visible at the hump of the wave, while the low-pressure region is visible at the hollow.

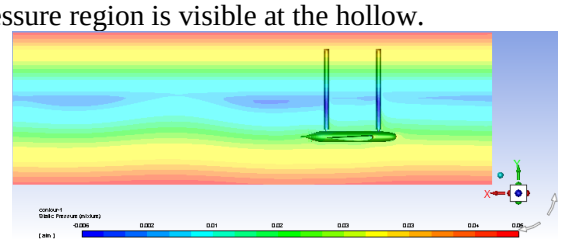

Figure 24. Static pressure (atm) distribution, $\frac{h}{d} = 3.6$, and Fn = 0.35

The values of resistance on the struts, Fs, and on the body without struts, Fb, as well as the resistance of the body attached to the struts, Fbs, are provided in tables (8), (9), and (10). The resistance values obtained from the test of the body model attached to the struts in the towing tank are also provided in the same table (10). Figure (25) depicts the trend of variations in resistance values determined by the CFD method and their differences from model test values in the towing tank. The maximum error of results derived from CFD and model testing for three depth-to-diameter ratios from low to high is equivalent to 11.91 percent, 6.51 percent, and 7.27 percent, respectively, in the table (11), assuming the basis of laboratory data values. Based on the CFD results, the values of induced resistance due to the presence and connection of the struts to the vessel body are computed in the table (12). It can be seen that the values of induced resistance grow as the depth-to-diameter ratio is increased in a fixed Froude number and that this trend increases as the Froude number is increased in a constant depth-to-diameter ratio.

Furthermore, for three depth-to-diameter ratios ranging from low to high, the maximum share of strut resistance from total resistance is 56.5 percent, 59 percent, and 62 percent, respectively, indicating that struts' existence is a significant role in the total resistance force. Similarly, for three low to high depth-to-diameter ratios, the contribution of the induced resistance due to the attachment of the struts to the body is equal to 33 percent, 41 percent, and 40 percent, respectively. As a result, the struts and their attachment to the main vessel body account for most of the total resistance.

Table 8. struts resistance

V (m/s)	F_d (N)		
	$\frac{h}{d}=7.7$	$\frac{h}{d}=9.7$	$\frac{h}{d}=11.2$
0.2	0.086	0.10	0.12
0.4	0.33	0.41	0.49
0.6	0.78	0.98	1.14
0.8	1.50	1.84	2.11
1	2.34	2.91	3.21
1.2	3.24	3.86	4.76

Table 9. body resistance

V (m/s)	F_d (N)		
	$\frac{h}{d}=3.6$	$\frac{h}{d}=4.5$	$\frac{h}{d}=5.2$
0.2	0.048	0.048	0.048
0.4	0.13	0.13	0.14
0.6	0.29	0.29	0.27
0.8	0.48	0.51	0.44
1	0.69	0.69	0.69
1.2	1.00	1.08	0.83

Table 10. body attached to struts resistance

V (m/s)	F_d (N) (cfd)			F_d (N) (experiment)		
	$\frac{h}{d}=3.6$	$\frac{h}{d}=4.5$	$\frac{h}{d}=5.2$	$\frac{h}{d}=3.6$	$\frac{h}{d}=4.5$	$\frac{h}{d}=5.2$
0.2	0.19	0.23	0.28	0.20	0.24	0.291
0.4	0.69	0.91	1.02	0.71	0.97	1.1
0.6	1.49	2.01	2.01	1.5	2.15	2.1
0.8	2.65	3.15	3.51	2.9	3.2	3.6
1	4.14	4.92	5.82	4.7	5.05	5.7
1.2	5.80	6.77	7.73	6.1	6.9	7.67

Table 11. error% based on experimental data

V (m/s)	Error%		
	$\frac{h}{d}=3.6$	$\frac{h}{d}=4.5$	$\frac{h}{d}=5.2$
0.2	5	4.17	3.8
0.4	2.8	6.19	7.3
0.6	6.6	6.5	4.3
0.8	8.6	1.5	2.5
1	11.9	2.6	2.1
1.2	4.9	1.9	0.78

Table 12. induced resistance

V (m/s)	$F_i = F_{b,s} - (F_b + F_s)$ (N)		
	$\frac{h}{d}=3.6$	$\frac{h}{d}=4.5$	$\frac{h}{d}=5.2$
0.2	0.056	0.082	0.112
0.4	0.23	0.37	0.39
0.6	0.42	0.74	0.6
0.8	0.67	0.8	0.96
1	1.11	1.32	1.92
1.2	1.56	1.83	2.14

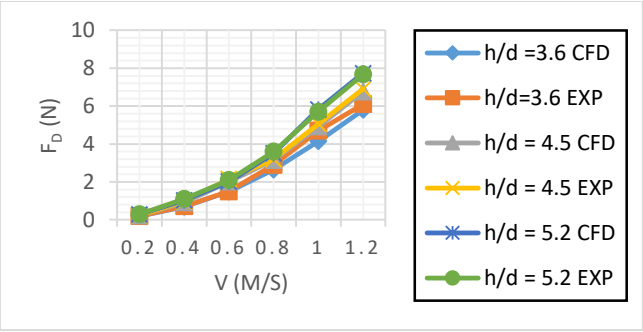

Figure 25. body attached to the struts resistance variations versus advance velocity, comparison between CFD results and experimental data in three depth ratios

7. Conclusion

Using Abies wood and CNC machining in 1: 1 scale, a model of a solar-powered AUV with panels attached to its two large wings was built. The model was fitted with two struts connected to a two-component transducer. The model was tested in the towing tank of the National Marine Laboratory of Iran (NIMALA) at three different depths and six different velocities in straight-line motion with one degree of freedom. Lead was added to the vessel to submerge it. The flow pattern created at the free surface and surrounding the model, as well as the force resistance on the model, were investigated. A model of the vessel was utilized to solve the unsteady flow around the body and struts using the standard k - ε turbulence model and standard wall function near-wall treatment in the ANSYS FLUENT 18 commercial software. Three steps are included in the simulations. In the first stage, two struts were simulated at three different depths and six velocities, according to the sizes provided by the laboratory as mentioned above, and simulation findings were derived. The vessel body was not attached to the struts in the following phase, which was solved and simulated, and the results were obtained. In the third phase, the vessel body was attached to the struts, and the solution results were compared to laboratory data. After that, the induced resistance forces due to the struts' connection to the vessel body were calculated. All three steps illustrate the waveform patterns generated around the simulated model. The following conclusions can be drawn:

- The resistance decreases as the depth of the body without the struts increases, but the drop is insignificant. This indicates that as the depth grows, the free surface effect shown in wave-making resistance reduces; nevertheless, because even the most minor depth-to-diameter ratio exceeds three times the diameter of the vessel hull, the impacts of wave resistance are not as significant. The value of resistance grows with increasing depth while solving the struts separately and the body attached to the struts. This is due to increased struts' wetted surface and the viscous resistance force's dominance over the pressure resistance force. In addition, as depth increases, the turbulence of the wave created on the free surface decreases.
- The amount of lift force is highly influenced by the wave pattern created on the free surface due to the giant wing's wide span compared to the body's size. The pressure on the wing's upper surface is increased by the hump portions, while the hollow parts reduce the pressure. The trend of lift force changes has increased with a relatively mild slope before the Reynolds number, but then it quickly rises. This is due to the flow regime crossing the turbulent area, which slows separation on the wings while also carrying a lot of momentum.
- In each of the three stages, the resistance force changes upwardly. The nonlinearity of resistance force behavior in free-surface flows causes the resistance force values to approach the initial values in some circumstances, even with the growing Froude number, as seen in the process of adjusting the resistance force for the struts independently.
- The maximum percentage of struts in the total resistance force is 62 percent, implying that it has higher values in the higher depth-to-diameter ratio. This large quantity indicates that the strut motion-induced wave-making resistance force accounts for a significant portion of the total resistance force. The generated resistance effect, caused by struts and their attachment to the body, also plays a significant role. According to the current study data for the analyzed model, the maximum is around 41 percent.

7. References

1- Russell B. Wynn ,Veerle A.I. Huvenne Veerle A.I.HuvenneaTimothy P.Le BasaBramley J.MurtonaDouglas, P.ConnellyaBrian, J.BettaHenry, A.RuhlaKirsty J.MorrisaJeffrey, PeakallbDaniel, R.ParsonscEsther, J.SumnerdStephen, E.DarbyeRobert, M.DorrellbJames, E.Hunta, (June 2014) *Autonomous Underwater Vehicles (AUVs): Their past, present and future contributions to the advancement of marine geoscience* Marine Geology, Volume 352, 1, Pages 451-468.

2- Patch A. David, (2000) *A Solar Energy System for Long-Term Deployment of AUV's* International Unmanned Undersea Vehicle Symposium.

3- Jalbert J, Baker J, Duchesney J, (2004) *Solar-Powered Autonomous Under Water Vehicle Development* Falmouth Scientific, Inc.

4- Ageev. MD, D.R. Blidberg, J. Jalbert, C.J. Melchin., (2002) *Results of the evaluation and testing of the solar powered AUV and its subsystems* Conference: Autonomous Underwater Vehicles.

5- Blidberg, D. Richard, Chappell, Steven, Jalbert, James C, (July 5-7, 2004) *Long endurance sampling of the ocean with solar powered AUV's* 5th IFAC/EURON Symposium on Intelligent Autonomous Vehicles, Instituto Superior Técnico, Lisboan, Portugal.

6- Denise M. Crimmins, Christopher T. Patty, Michael A. Beliard, John Baker, James C. Jalbert, Rick J. Komerska, Steven G. Chappell, D.

Richard Blidberg.(2006) *Long-Endurance Test Results of the Solar-Powered AUV System* Conference: OCEANS.

7- Razmjoo.Ali, Mohammad Ghadimi, Mehrzad Shams, Hoseyn Shirmohammadi,(October 2015), *Design and Built a Research AUV Solar Light Weight* International Journal of Energy and Power Engineering, Volume 4, Issue 5, Pages: 268-274.

8- Polish,C.,Ranmuthugala,D.,Duffy,J. andRenilson,M.,(2011) *Characterisation of near surface effects acting on an underwater vehicle within the vertical plane*, Australian Maritime College.

9- Neulist, D, (2011), *Experimental Investigation into the Hydrodynamic Characteristics of a Submarine Operating Near the Free Surface*, Australian Maritime College, Launceston.

10- Salari.Mahmoud, Rava.Amin, (2017) *Numerical investigation of hydrodynamic flow over an AUV moving in the water-surface vicinity considering the laminar-turbulent transition* Journal of Marine Science and Application

11- Javanmard.E, Mansoorzadeh. Sh. (2019) *A Computational Fluid Dynamics Investigation on the Drag Coefficient Measurement of an AUV in a Towing Tank* Journal of Applied Fluid Mechanics.

12- Asadi Asrami. E, Moonesun. M, Azizi Abi. F, (2021) *CFD and Experimental Hydrodynamic Analysis of a Solar AUV* CAMES, 28, doi: 10.24423/cames.301 ONLINE FIRST March 18.

13- Mohammad Moonesun, Ehsan Asadi Asrami, Julia Bodnarchuk (2021) *Hydrodynamic Analysis on the Body of a Solar Autonomous Underwater Vehicle by Numerical Method* World Academy of Science, Engineering and Technology.

14- Mohammad Moonesun, Firouz Ghasemzadeh, Yuri Korol, Valeri Nikrasov, Alexi Yastreba, Alexander Ursolov, Asghar Mahdian, (2016) *Technical Notes on the Near Surface Experiments of Submerged Submarine* INTERNATIONAL JOURNAL OF MARITIME TECHNOLOGY.

15- Ariful Hoque. Md, Mashud Karim, Aevelina Rahman (2017) *Simulation of Water Wave Generated by Shallowly Submerged Asymmetric Hydrofoil* Procedia Engineering.

16- Mashud Karim.Md., BijoyPrasad, NasifRahman. (2014) *Numerical simulation of free surface water wave for the flow around NACA 0015 hydrofoil using the volume of fluid (VOF) method* Ocean Engineering.

17- Prasad.Bijoy, Takanori Hino, Kazuo Suzuki. (2015) *Numerical simulation of free surface flows around shallowly submerged hydrofoil by OpenFOAM* Ocean Engineering.

18- Roddy.Robert.F. (September 1990) *Investigation of the Stability and Control Characteristics of Several Configurations of the DARPA SUBOFF Model (DTRC MODEL 5470) from Captive-Model Experiment.*

19- Divsalar.K. (2019) *Improving the hydrodynamic performance of the SUBOFF bare hull model: a CFD approach* Acta Mechanica Sinica.

20- Hirt, C.W, Nichols,B.D, (1981) *Volumeof fluid (VOF) method for the dynamics of free boundaries* J.Comput.Phy.39(1),201–225.

21- Azcueta R, (2003) *Steady and unsteady RANSE simulations for planning craft*. FAST: the 7th international conference on Fast Sea transportation. Ischia, Italy

22- De Luca F, Mancini S,Miranda S, Pensa C (2016) *An extended verification and validation study of CFD simulations for planing hulls.* J Ship Res 60(2):101–118.